ACS APPLIED MATERIALS & INTERFACES

RESEARCH ARTICLE

www.acsami.org

Three-Dimensional Hierarchical Flowerlike α-Fe_2O_3 Nanostructures: Synthesis and Ethanol-Sensing Properties

LiLi Wang, Teng Fei,* Zheng Lou, and Tong Zhang*

State Key Laboratory on Integrated Optoelectronics, College of Electronic Science, Engineering, Jilin University, Changchun 130012, People's Republic of China

ABSTRACT: The α-Fe_2O_3 hierarchical nanostructures have been successfully synthesized via a simple solvothermal method. The as-prepared samples are loose and porous with flowerlike structure, and the subunits are irregularly shaped nanosheets. The morphology of the α-Fe_2O_3 structures was observed to be tunable as a function of reaction time. To demonstrate the potential applications, we have fabricated a gas sensor from the as-synthesized hierarchical α-Fe_2O_3 and investigated it for ethanol detection. Results show that the hierarchical α-Fe_2O_3 sensor exhibits significantly improved sensor performances in comparison with the compact α-Fe_2O_3 structures. The enhancement of sensing properties is attributed to the unique porous and well-aligned nanostructure.

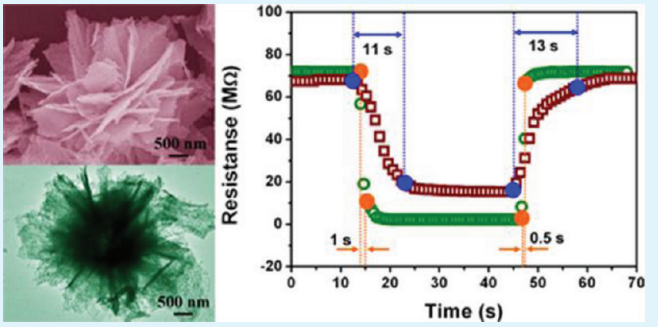

KEYWORDS: α-Fe_2O_3, hierarchical structures, rapid response, gas sensor

1. INTRODUCTION

With the advancement in materials science, hierarchical structures materials open a new horizon for the investigation of high-performance sensors, and are considered as good candidates for gas sensors because of their low density and large surface-area-to-volume ratio than solid structures.[1−4] To date, many types of hierarchical superstructures have been successfully fabricated by a variety of methods.[5−9] However, these methods usually hold disadvantages related to high temperatures or tedious synthetic procedures, which possibly result in the increased cost and limited the potential applications. Therefore, exploration of a simple, mild and economical approach is strongly desirable for the fabrication of hierarchical nanostructures.[10−15] Nevertheless, in spite of extensive research efforts, synthesis of hierarchical structures by a simple solvothermal route still remains a technological challenge.

Hematite (α-Fe_2O_3), an n-type semiconductor (E_g = 2.1 eV), is the most thermodynamically stable phase of iron oxide under ambient conditions with low cost, high resistance to corrosion and environment-friendly features. It has been extensively investigated for various applications, such as catalysts, gas sensor, electronic materials, magnetic devices, biological and medical fields.[16−21] Stimulated by these intriguing properties and broad applications, well-defined nanostructures of iron oxides with different dimensionalities such as 0D (nanoparticles),[22] 1D (nanorods, nanowires, nanotubes,[23,24] 2D/3D (nanorings, nanobelts, nanocubes, as well as hollow and porous nanostructures)[25,26] have been successfully obtained. Until now, the simple synthesis strategy for the flowerlike α-Fe_2O_3 hierarchical structures is still rarely reported.

In this work, we report a simple strategy for the synthesis of flowerlike α-Fe_2O_3 hierarchical structures through a solvothermal process with subsequent calcination of the obtained precursor. The obtained α-Fe_2O_3 hierarchical architectures consisted of a number of two-dimensional (2D) nanosheets. The formation mechanism as investigated in detail. A comparative gas sensing study between the as-synthesized α-Fe_2O_3 hierarchical architectures and α-Fe_2O_3 compact structures was performed to demonstrate the excellent gas sensing properties of α-Fe_2O_3 hierarchical materials.

2. EXPERIMENTAL SECTION

2.1. Materials. All the reagents were of analytical grade and used without further purification. Ferric chloride ($FeCl_3 \cdot 6H_2O$), urea, ethylene glycol and glycerol were purchased from Sinopharm Chemical Reagent Co. (Shanghai, China).

2.2. Synthesis Process. Flowerlike α-Fe_2O_3 hierarchical structures was prepared through a two-step process including solvothermal synthesis of FeOOH precursor and calcination of the obtained precursor. In a typical experiment, 0.15 g of $FeCl_3 \cdot 6H_2O$ and 0.2 g of urea were mixed with 25 mL of ethylene glycol under magnetic stirring vigorously until a uniform suspension was formed. The suspension was then transferred into a 40 mL teflon-lined stainless steel autoclave. After sealing, the autoclave was heated at 160 °C for 8 h, and then cooled naturally. The product was collected by centrifugation, washed with deionized water and absolute ethanol several times, and finally dried in vacuum at 60 °C for 6 h. The dried powder of the precursor was heated in air from room temperature to 500 °C

Received: August 18, 2011
Accepted: November 5, 2011
Published: November 06, 2011

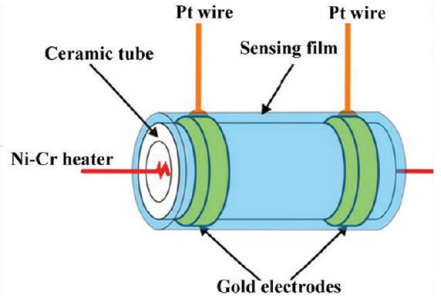

Figure 1. Schematic structure of the gas sensor.

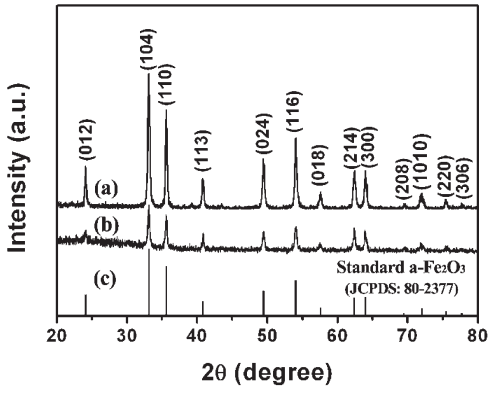

Figure 2. XRD pattern of (a) flower-\like α-Fe_2O_3 structures, (b) compact α-Fe_2O_3 structures, and (c) standard XRD pattern of α-Fe_2O_3 (JCPDS No. 80-2377).

at a heating rate of 5 °C min^{-1} and then kept at 500 °C for 10 min. After the furnace was cooled to room temperature, and the red α-Fe_2O_3 hierarchical product was obtained. Detailed synthesis procedures of the α-Fe_2O_3 compact structures were the same as those for making α-Fe_2O_3 hierarchical structures, except the ethylene glycol changed to be glycerol.

2.3. Characterization. The reaction products were characterized by X-ray diffraction (XRD) using a Rigaku D/Max-2550 diffractometer with Cu Kα radiation (λ = 0.154 18 nm) (40 kV, 350 mA) in the range of 20−80° (2θ) at a scanning rate of 10° min^{-1}. Field emission scanning electron microscope (FESEM: SHIMADZU Japan, SSX-550) images of hierarchical α-Fe_2O_3 were also taken. TEM and HRTEM images were recorded with a Tecnai G^2 20S-Twin transmission electron microscope operating at an accelerating voltage of 120 and 200 kV, respectively. The Brunauer−Emmett−Teller (BET) specific surface areas (SBET) were calculated using the BET equation. Desorption isotherm was used to determine the pore size distribution using the Barret−Joyner−Halender (BJH) method.

2.4. Fabrication and Measurement of Gas Sensor. The products were mixed with deionized water at a weight ratio of 4:1 to form a paste. The sensors were made by coating ceramic tube with the paste to form a thin 10 μm sensing film. A pair of gold electrodes was installed at each end of the ceramic tube before it was coated with the paste; each electrode was connected with two Pt wires. A Ni−Cr heating wire was inserted into the tube to form an indirect-heated gas sensor. The structure of the sensor is shown in Figure 1. The details of the sensor fabrication are similar to those reported in the literature.[27]

The electrical properties of the sensor were measured by a RQ-2 series Intelligent Test Meter (China). The response ($S = R_a/R_g$) of the sensor was defined as the ratio of sensor resistance in dry air (R_a) to that in a target gas (R_g) between 210 and 350 °C. The time taken by the resistor to range from R_a to R_a − 90% ($R_a - R_g$) is defined as the response time, τ_{res}, when the sensor is exposed to the target gas. The time taken by the resistor to change from R_g to R_g + 90% ($R_a - R_g$) is defined as the recovery time, τ_{recov}, when the sensor is retrieved from the target gas.

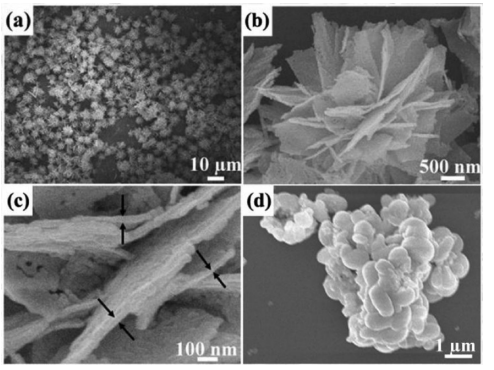

Figure 3. FESEM images of flower-like α-Fe_2O_3 nanostructure: (a) lower magnification; (b, c) higher magnification. (d) FESEM images of the compact α-Fe_2O_3 nanostructure.

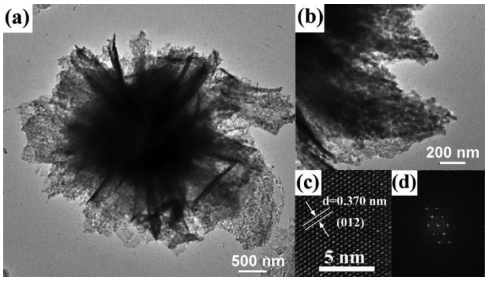

Figure 4. (a) Low-magnification and (b) high-magnification TEM, and (c) HRTEM images of α-Fe_2O_3 flowerlike nanostructures; (d) the corresponding FFT of the HRTEM image.

3. RESULTS AND DISCUSSION

3.1. Structural and Morphological Characteristics. The corresponding powder XRD pattern (Figure 2) provides crystalline and phase information for the obtained products. Spectra a and b in Figure 2 are the XRD patterns of the flowerlike and compact α-Fe_2O_3 products that prepared at 160 °C, where all the diffraction peaks can be indexed to pure α-Fe_2O_3 (JCPDS no. 80-2377) (Figure 2c). The intense peaks of the XRD pattern indicate that the α-Fe_2O_3 product was well crystallized. In addition, no impurities peaks from any other impurities were detected by XRD, indicating the high purity of the products.

The morphologies and nanostructures of the calcined products were illuminated by FESEM observations. The lower magnification of the FESEM images in Figure 3a show that a typical sample is composed of numerous flower-like α-Fe_2O_3 nanostructures, which maintain well-preserved hierarchical structures with diameters of 5-6 μm. A typical flowerlike nanostructure is shown in the magnified FESEM image in Figure 3b, and more details can be found in Figure 3c, which demonstrate that the exterior of each flowerlike hierarchical nanostructure is

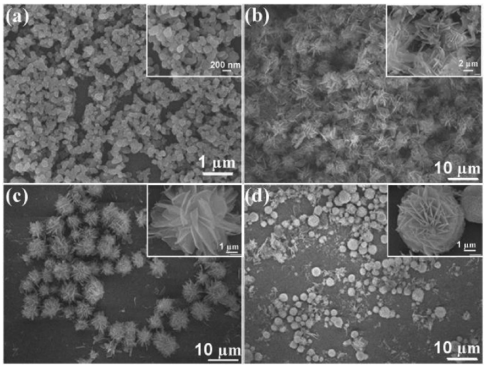

Figure 5. Series of SEM images of the as-prepared products at 160 °C with different times: (a)1, (b) 4, (c) 8, and (d) 12 h. The insets are corresponding high-magnification SEM images.

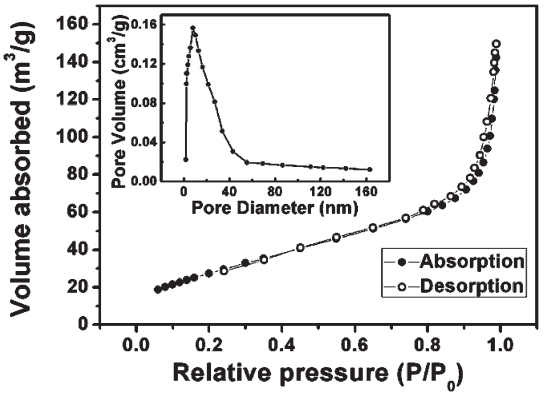

Figure 6. N_2 adsorption−desorption isotherm and pore size distribution (inset) of the α-Fe_2O_3.

composed of abundant randomly assembled irregular-shaped nanosheets with a thickness of about 30 nm (black arrow), as well as loose and cross-linked interiors. In contrast, compact α-Fe_2O_3 nanostructures with a smooth surface were prepared from a glycerol solution (Figure 3d).

More-detailed structural information of the α-Fe_2O_3 nanocrystals was provided by TEM. Figure 4a displays a typical TEM image of an as-prepared product at low magnification, which illustrates that the sample is mainly made up of abundant randomly thin nanosheets. Figure 4b shows a high-magnification TEM image of a part of single α-Fe_2O_3 hierarchical nanostructure, indicating that the structures of the flowerlike α-Fe_2O_3 hierarchical structures are very loose, and the nanosheets are mainly composed of irregular-shaped nanoparticles. It also can be seen that there are some pale areas between the dark nanoparticles, which indicates the existence of porous nanostructures on the nanosheet (Figure 4b). The HRTEM image of the α-Fe_2O_3 hierarchical nanostructures (Figure 4c) shows the lattice image obtained at the edge of the particle. The typical lattice fringe spacing is determined to be 0.370 nm, corresponding to the (012) d spacing of the α-Fe_2O_3, which clearly demonstrate that the hierarchical nanostructures consist of the single crystalline nanoparticles. The hexagonal-like spot arrays (Figure 4d) are shown by the fast fourier transform spectrum further verifies the single-crystal nature of the nanoparticles and hexagonal crystal structure of the α-Fe_2O_3.

To understand the role reaction time play in controlling the morphology of the product, we have synthesized nanostructures at 160 °C with different times. The other experimental details are the same as with the products in Figure 3, and the corresponding results are shown in Figure 5. At the early stage (1 h), it can be seen that the product is composed of nanoparticles with a diameter of about 100 nm (Figure 5a and the inset). After reaction for 4 h, the nanoparticles nearly disappeared and the products transformed into thin nanosheets (Figure 5b and the inset). As the reaction time increased to 8 h, we found that oriented aggregation happened and many nanosheets self-assembled into form a neatly flower-like nanostructures with loose interiors structures (Figure 5c and the inset), and the detailed characteristics of them were described previously. Interestingly, when the treatment was increased to 12 h, these loose flowerlike nanostructures transform into the hierarchical and dense spheres with a diameter of about 4−7 μm as shown in Figure 5d and the inset.

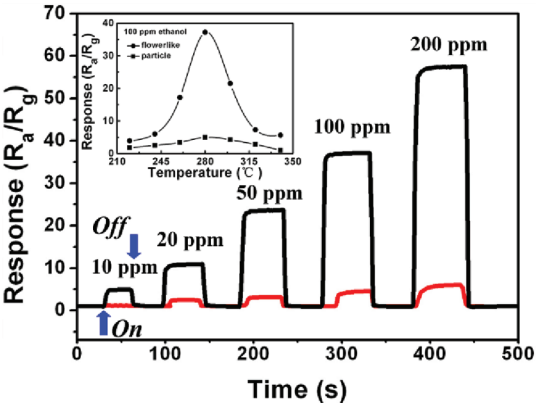

Figure 7. Response of α-Fe_2O_3 hierarchical structures (black line) and α-Fe_2O_3 compact structures (red line) sensors to ethanol with different concentration. The inset is response versus operating temperature of the hierarchical α-Fe_2O_3 sensor exposed to 100 ppm ethanol.

The nitrogen adsorption−desorption isotherms were measured to determine the specific surface area and pore volume of as-prepared flowerlike α-Fe_2O_3 hierarchical structures, and the corresponding results were presented in Figure 6. The pore size distribution, derived from desorption data and calculated from the isotherm using the BJH model, shows that the average pores of such a sample are around 4-50 nm. The Brunauer−Emmett−Teller (BET) specific surface area of the sample calculated from N_2 adsorption is 107 $m^2\ g^{-1}$, which is much larger than of the compact α-Fe_2O_3 structures (17 $m^2\ g^{-1}$). The large surface area and porous framework of the α-Fe_2O_3 hierarchical material provide efficient transport pathways to their interior voids, which make potentially useful for application such as gas sensor.

3.2. Ethanol Sensing Properties. It is common knowledge that hierarchical nanostructures materials are considered as good candidates for gas sensing applications because of their large surface area to volume and mesoporosity.[3,28] Therefore, we have fabricated two different gas sensors from the prepared hierarchical α-Fe_2O_3 nanostructures and compact α-Fe_2O_3 structures, and ethanol is tested as a probe molecule to examine the sensor properties. Figure 7 shows the dynamic response−recovery curves of the two sensors to different ethanol concentrations (10−200 ppm). It can be seen that the flower-like α-Fe_2O_3 sensor displayed about

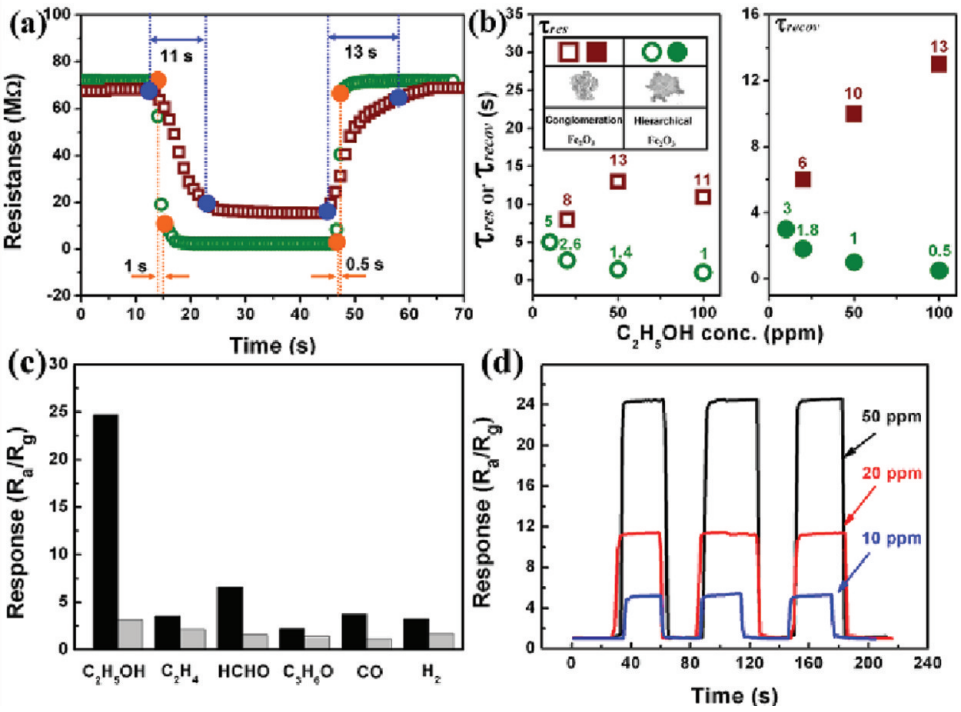

Figure 8. (a) Dynamic ethanol sensing transient of the flowerlike α-Fe_2O_3 (○) and compact α-Fe_2O_3 (□); (b) response time (τ_{res}) and recover time (τ_{recov}); (c) selectivity of the flowerlike α-Fe_2O_3 and compact α-Fe_2O_3 sensors on successive exposure to 50 ppm of C_2H_5OH, C_2H_4, HCHO, C_3H_6O, CO, H_2 at 280 °C; (d) reproducibility of the flowerlike α-Fe_2O_3 sensor on successive exposure (3 cycles) to 10, 20, and 50 ppm of ethanol.

Table 1. Gas Responses to C_2H_5OH of the α-Fe_2O_3 Sensors in the Present Study and Those Reported in the Literature

materials	size	ethanol (ppm)	temperature (°C)	response time (s)	recovery time (s)
this work	5−6 μm	50	280	1	0.5
a-Fe_2O_3[29] nanoparallelepipeds	220 nm	50		5	6
a-Fe_2O_3[21] hierarchical architectures	5 μm	50	250	5	10
a-Fe_2O_3[30] nanoparticles	58 nm	30		20	50
a-Fe_2O_3[31] microcubes	1 μm	50	320	6	2
a-Fe_2O_3[32] nanobelts	400 nm	50	285	10	24
a-Fe_2O_3[33] nanoparticles	7 nm	1000	270	20	100
Fe_2O_3[34] nanorods	900 nm	50	150	3	8
a-Fe_2O_3[35] hollow sea urchin slructurcs	2−4.5 μnm	100	350	21	14

ninefold enhancement in sensitivity compared with the compact one. The response amplitude of the flower-like α-Fe_2O_3 sensor is significantly increased with increasing ethanol concentration, while the increase in the response of the compact one is almost negligible. The inset of Figure 7 shows the response of two sensors at different temperatures. It can be seen that for 100 ppm of ethanol the maximum response values of two sensors are 37.9 and 4.7 at the optimal temperature of 280 °C, respectively. Thus, we choose 280 °C as our working temperature to proceed with the subsequent detections.

The response and recovery time of two sensors to 100 ppm of ethanol at 280 °C are shown in Figure 8a, b. As can be seen in Figure 8a, the τ_{res} and τ_{recov} of the hierarchical nanostructures to 100 ppm of ethanol are as short as 1 and 0.5 s, respectively, while that of compact structures are 11 and 13 s, respectively. The τ_{recov} value of the compact α-Fe_2O_3 are much longer (6−13 s) than that of the flower-like α-Fe_2O_3 hierarchical nanostructures range from 0.5 to 3 s (Figure 8a, b). The C_2H_5OH responses of various α-Fe_2O_3 nanostructures such as nanoparticles, nanowires, nanorods, hierarchical structures, and nanofibers in the literature were summarized in Table 1.[21,29−35] The C_2H_5OH response times of flowerlike α-Fe_2O_3 sensor in the present study were among the fastest values reported in the literature for α-Fe_2O_3 sensors. Figure 8c exhibits the response of the flowerlike α-Fe_2O_3 and compact α-Fe_2O_3 sensor at 280 °C to 50 ppm of various gas vapours, including C_2H_5OH, C_2H_4, HCHO, C_3H_6O, CO, and H_2. Clearly, the responses of the flowerlike α-Fe_2O_3 sensor to six gases are all improved compared with the compact one, and the largest increase is only observed for ethanol, implying the good selectivity of the sensor for ethanol. Stability, that is, the ability to successively respond to a target gas without a visible decrease in sensor response, is another important feature of chemical sensor. Figure 8d illustrates the reproducibility of the flowerlike α-Fe_2O_3 sensor, revealing that the sensor maintains its initial response amplitude without a clear decrease upon three successive sensing tests to 10, 20, and 50 ppm of ethanol.

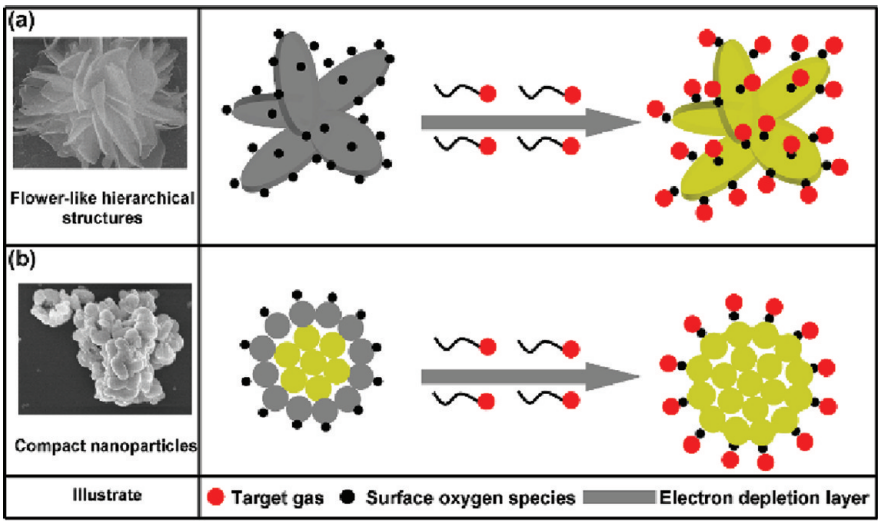

Figure 9. Schematic illustrations of two different sensor materials: (a) flowerlike hierarchical structures; (b) compact structures.

The improvement of the sensing performance of the α-Fe_2O_3 nanostructures may be attributed to the contribution of the contact surface area between α-Fe_2O_3 hierarchical structures and target gases.[36−38] It is believed that the response and recovery process involves serial reactions: adsorption-oxidation-desorption. Physically, the α-Fe_2O_3 hierarchical nanostructures (Figure 9a) composed of numerous nanosheets possess a loose and porous structure in comparison to the compact nanoparticles (Figure 9b). These unique loose structures can provide a large surface-to-volume ratio, which is of great benefit to gas diffusion and mass transport, thus leading to numerous oxygen molecules adsorbed onto the hierarchical α-Fe_2O_3 surface. Adsorbed oxygen can diffuse faster to surface vacancies and capture electrons from the conduction band of α-Fe_2O_3 to become oxygen ions (O^-, O^{2-}, O_2^-) (Figure 9a). This process increases both the quantity of adsorbed oxygen and the molecule-ion conversion rate, resulting in the greater and faster degree of electron depletion from the α-Fe_2O_3 hierarchical nanostructures. As shown in Figure 9, the depletion layer at the α-Fe_2O_3 hierarchical nanostructures interface is wider than that at the compact α-Fe_2O_3 structures surface. Here, the barriers at the nanosheets greatly block the electrons transporting, and the resistance of the sensors is very high (Figure 8a). When two sensors are exposed to the ethanol gas, the ethanol molecules are oxidized by the oxygen species on the surface, and the depleted electrons are fed back to the sample, so the resistance decreases (Figure 8a). As illustrated in Figure 9b, for the compact structures, it is theoretically difficult for target gases to diffuse into the interior of the sensing layer, thus sensing reactions can only happen on the outer surface and result in only one electron depletion layer. However, once the target gases diffuse into the interior of the sensing layer, it cannot easily diffuse out in the counter diffusion process of recovery, which may retard the recovery speed. Hierarchical structures with well-aligned porous structures and larger surface area have been reported previously.[1,3,39,40] It can be observed (in Figure 3c) that the flowerlike Fe_2O_3 hierarchical structures are very loose and the nanosheets with well-aligned porous structures. When sample units are exposed to the target gas, the gas is easy to spread inward by well-aligned porous structures; the gas diffusion toward the entire sensing surface is not hampered. Thus, the remarkably response and shorter sensor response time can be attributed to the rapid diffusion of the target gas toward the sensing surface via porous and well-aligned nanostructures. These results indicate that the as-prepared hierarchical porous α-Fe_2O_3 nanostructures are promising candidates for gas sensing application.

4. CONCLUSIONS

In summary, a simple solvothermal method combined with a subsequent annealing process was reported for the synthesis of porous flowerlike α-Fe_2O_3 hierarchical nanostructures. This porous flowerlike architecture is assembled by many interleaving nanosheets, which have thickness of about 30 nm. It was found that the reaction time plays an important role for the assembly process. Importantly, the as-obtained flowerlike α-Fe_2O_3 sensor exhibited excellent ethanol sensing performances at 280 °C and the quick response and recovery times are about 1 and 0.5 s to 100 ppm ethanol, respectively. On the basis of this solvothermal route and the gained unique nanostructures, it is significant for exploiting the synthesis of other semiconductors with novel shapes and particular applications.

AUTHOR INFORMATION

Corresponding Author

*E-mail: zhangtong@jlu.edu.cn (T.Z.); feiteng@jlu.edu.cn (F. T.). Tel.: +86 431 85168385. Fax: +86 431 85168270.

ACKNOWLEDGMENT

This research work was financially supported by the Natural Science Foundation Committee (NSFC, Grant 609710), and Project of Innovation Research Team of Jilin University (Grant 201004003).

REFERENCES

(1) Choi, K. I.; Kim, H. R.; Lee, J. H. *Sens. Actuators, B* **2009**, *138*, 497–503.

(2) Jia, L. C.; Cai, W. P.; Wang, H. Q.; Sun, F. Q.; Li, Y. *ACS Nano* **2009**, *3*, 2697–2705.

(3) Lee, J. H. *Sens. Actuators B* **2009**, *140*, 319–336.

(4) Xu, X. X.; Zhuang, J.; Wang, X. *J. Am. Chem. Soc.* **2008**, *130*, 12527–12535.
(5) Datta, A.; Panda, S. K.; Ganguli, D.; Mishra, P.; Chaudhuri, S. *Cryst. Growth Des.* **2007**, *7*, 163–169.
(6) Kim, S. W.; Kim, M.; Lee, W. Y.; Hyeon, T. *J. Am. Chem. Soc.* **2002**, *124*, 7642–7643.
(7) Shi, L.; Bao, K.; Cao, J.; Qian, Y. T. *CrystEngComm* **2009**, *11*, 2009–2014.
(8) Guan, L.; Pang, H.; Wang, J. J.; Lu, Q. Y.; Yin, J. Z.; Gao, F. *Chem. Commun* **2010**, *46*, 7022–7024.
(9) Yin, Y. D.; Erdonmez, C.; Aloni, S.; Alivisatos, A. P. *J. Am. Chem. Soc.* **2006**, *128*, 12671–12673.
(10) Bai, P.; Wu, P.; Yan, Z.; Zhou, J.; Zhao, X. S. *J. Phys. Chem. C* **2007**, *111*, 9729–9733.
(11) Leng, N.; Gao, L. Z.; Ping, F.; Zhang, J. Y.; Fu, X. Q.; Liu, Y. G.; Yan, X. Y.; Wang, T. H. *Small* **2006**, *2*, 621–625.
(12) Zhou, X.; Hu, Z.; Fan, Y.; Chen, S.; Ding, W.; Xu, N. *J. Phys. Chem. C* **2008**, *112*, 11722–11728.
(13) Chen, X. Y.; Wang, X.; Wang, Z. H.; Yang, X. G.; Qian, Y. T. *Cryst. Growth Des.* **2005**, *5*, 347–350.
(14) Liu, J. P.; Huang, X. T.; Li, Y. Y.; Sulieman, K. M.; He, X.; Sun, F. L. *Cryst. Growth Des.* **2006**, *6*, 1690–1696.
(15) Liu, J. P.; Huang, X. T.; Sulieman, K. M.; Sun, F. L.; He, X. *J. Phys. Chem. B* **2006**, *110*, 10612–10618.
(16) Sugimoto, T.; Sakata, K. *J. Colloid Interface Sci.* **1992**, *152*, 587–590.
(17) Jain, G.; Balasubramanian, M.; Xu, J. *J. Chem. Mater.* **2006**, *18*, 423–424.
(18) Hermanek, M.; Zboril, R.; Medrik, I.; Pechousek, J.; Gregor, C. *J. Am. Chem. Soc.* **2007**, *129*, 10929–10936.
(19) Cesar, I.; Kay, A.; Gonzalez Martinez, J. A.; GrRtzel, M. *J. Am. Chem. Soc.* **2006**, *128*, 45824583.
(20) Wu, P.; Wang, W.; Huang, Y.; Shen, H.; Lo, Y.; Tsai, T.; Shieh, D.; Yeh, C. *Chem.—Eur. J.* **2007**, *13*, 3878–3885.
(21) Hao, Q. Y.; Liu, S.; Yin, X. M.; Du, Z. F.; Zhang, M.; Li, L. M.; Wang, Y. G.; Wang, T. H.; Li, Q. H. *CrystEngComm* **2011**, *13*, 806–812.
(22) Taniguchi, T.; Nakagawa, K.; Watanabe, T.; Matsushita, N.; Yoshimura, M. *J. Phys. Chem. C* **2009**, *113*, 839–843.
(23) (a) Tang, B.; Wang, G.; Zhuo, L.; Ge, J.; Cui, L. *Inorg. Chem.* **2006**, *45*, 5196–5200. (b) Hu, X.; Yu, J. *Adv. Funct. Mater.* **2008**, *18*, 880–887.
(24) Nasibulin, A.; Rackauskas, S.; Jiang, H.; Tian, Y.; Mudimela, P.; Shandakov, S.; Nasibulina, L.; Jani, S.; Kauppinen, E. *Nano Res.* **2009**, *2*, 373–379.
(25) Jia, C.; Sun, L.; Luo, F.; Han, X.; Heyderman, L.; Yan, Z.; Yan, C.; Zheng, K.; Zhang, Z.; Takano, M. *J. Am. Chem. Soc.* **2008**, *130*, 16968–16977.
(26) Casula, M.; Jun, Y.; Zaziski, D.; Chan, E.; Corrias, A.; Alivisatos, A. *J. Am. Chem. Soc.* **2006**, *128*, 1675–1682.
(27) Zeng, Y.; Zhang, T.; Wang, L. J.; Wang, X.; Kang, M. H.; Fan, H. T.; Wang, R.; He, Y. *Sens. Actuators, B* **2006**, *140*, 73–78.
(28) Mullin, J. W.; *Crystallization*, 3rd ed.; Butterworth-Heinemaan: Oxford, U.K., 1997.
(29) Li, X. L.; Wei, W. J.; Wang, S. Z.; Kuai, L.; Geng, B. Y. *Nanoscale* **2011**, *3*, 718–724.
(30) Huo, L. H.; Li, Q.; Zhao, H.; Yu, L. J.; Gao, S.; Zhao, J. G. *Sens. Actuators B* **2005**, *107*, 915–920.
(31) Xiong, S.; Xu, J.; Chen, D.; Wang, R. M.; Hu, X. L.; Shen, G. Z.; Wang, Z. L. *CrystEngComm* **2011**, DOI: 10.1039/c1ce05569k.
(32) Fan, H. T.; Zhang, T.; Xu, X. J.; Lv, N. *Sens. Actuators B* **2011**, *153*, 83–88.
(33) Jing, Z. H. *Mater. Lett.* **2006**, *60*, 3315–3318.
(34) Gou, X. L.; Wang, G. X.; Kong, X. Y.; Wexler, D.; Horvat, J.; Yang, J.; Park, J. *Chem.—Eur. J.* **2008**, *14*, 5996–6002.
(35) Zhang, F. H.; Yang, H. Q.; Xie, X. L.; Li, L.; Zhang, L. H.; Yu, J.; Zhao, H.; Liu, B. *Sens. Actuators, B* **2009**, *141*, 381–389.
(36) Yao, W. T.; Yu, S. H.; Liu, S. J.; Chen, J. P.; Liu, X. M.; Li, F. Q. *J. Phys. Chem. B* **2006**, *110*, 11704–11710.
(37) Lu, H. B.; Wang, S. M.; Zhao, L.; Li, J. C.; Dong, B. H.; Xu, Z. X. *J. Mater. Chem.* **2011**, *21*, 4228–4234.
(38) Li, C. C.; Yin, X. M.; Li, Q. H.; Wang, T. H. *CrystEngComm* **2011**, *13*, 1557–1563.
(39) Sun, S.; Wang, W.; Xu, H.; Zhou, L.; Shang, M.; Zhang, L. *J. Phys. Chem. C* **2008**, *112*, 17835–17843.
(40) Zhang, Y.; He, X. L.; Li, J. P.; Zhang, H. G.; Gao, X. G. *Sens. Actuators, B* **2007**, *128*, 293–298.